Nuclear Inst. and Methods in Physics Research B 461 (2019) 159–165

Contents lists available at ScienceDirect

Nuclear Inst. and Methods in Physics Research B

journal homepage: www.elsevier.com/locate/nimb

Comparison of dynamic deuterium retention in single-crystal and poly-crystals of tungsten: The role of natural defects

F. Ghiorghiu[a,1], M. Minissale[a,1], E.A. Hodille[a], C. Grisolia[b], T. Angot[a], R. Bisson[a,*]

[a] Aix Marseille Univ, CNRS, PIIM, Marseille, France
[b] CEA, IRFM, 13018 Saint-Paul-lez-Durance, France

ARTICLE INFO

Keywords:
Tungsten
Deuterium
Ion
Plasma facing components
Fusion
Macroscopic rate equation

ABSTRACT

The time evolution of fuel retention in materials relevant for future fusion reactors is compared for two different tungsten microstructures: single-crystal versus recrystallized poly-crystals. The initial retention of both types of sample is similar. It decays exponentially with a time constant of ~18 h at 300 K (the so-called short-term retention). After 48 h at room temperature, a constant deuterium retention is measured (long-term retention) with the single-crystal containing systematically less deuterium than poly-crystals. Macroscopic rate equations models are built with density functional theory inputs to reproduce deuterium desorption observables with the MHIMS-R code. We found that the native oxide layer could explain the desorption peak located at ~450 K as well as most of the short-term retention in the single-crystal. The native oxide together with, dislocations for single-crystal and grain boundaries for poly-crystals, are responsible for the long-term retention. Dislocations should explain the desorption peak located at ~815 K for mechanically polished samples. The dual role of most of tungsten defects is related to their multi-trapping properties with filling-level-dependent detrapping energies. Finally, the use of an effective diffusivity of deuterium through the native oxide layer, i.e. its diffusion barrier character, is evaluated.

1. Introduction

Thermal properties of tungsten (W) make it a suitable material for plasma facing components (PFCs) in fusion devices such as ITER and DEMO [1–3]. Nevertheless, the high particle fluxes (up to 10^{24} m^{-2} s^{-1}) expected in the W-based PFC (e.g. in the divertor) could lead to a significant fuel retention. Fuel particles (i.e. deuterium and tritium) implanted in PFCs can diffuse and be trapped at tungsten defects. The presence of tritium in defective PFCs causes nuclear safety issues due to regulation-limited amount of tritium in the in-vessel components (700 g in ITER [4,5]). Even though retention in beryllium is expected to be dominant in ITER, current plans consider DEMO to have a complete tungsten first-wall. Moreover, for economic issues, tritium needs to be retrieved from walls in order to be recycled due to its low abundance on Earth. For such reasons, diffusion, trapping and detrapping of deuterium in W have been extensively studied experimentally and theoretically in the last two decades [6–9] (and references therein).

Usually hydrogen retention is studied experimentally through temperature-programmed desorption (TPD) and nuclear reaction analysis (NRA). Retention in W is induced by different trapping mechanisms with activation energies for detrapping up to 2.1 eV as deduced from experiments [6]. Experimental results are usually analyzed with macroscopic rate equations (MRE) models [10–16] that allow to determine (de)trapping parameters useful to predict the retention of hydrogen isotopes in tungsten materials [17]. However, it is still a matter of debate which quantitative role is played by each type of defects in realistic W materials.

In recent years, density functional theory (DFT) studies have shown that all tungsten defects (grain boundaries [18,19], dislocation loops [19], vacancies [20–23], oxygen-vacancy clusters [24] …) can contribute to hydrogen isotopes retention. Leveraging this new knowledge in an experimental-modeling joint study [25], we showed that two (de) trapping mechanisms were necessary to reproduce various desorption observables related to a single desorption peak in recrystallized poly-crystalline tungsten. Using DFT inputs to feed various MRE models, we found that these two (de)trapping mechanisms should be related to grain boundaries and the tungsten surface native oxide. The purpose of the present study is to characterize further the deuterium retention in pristine tungsten assessing the importance of tungsten natural defects, i.e. defects that are present in tungsten after manufacturing (grain

* Corresponding author.
E-mail address: regis.bisson@univ-amu.fr (R. Bisson).
[1] These authors contributed equally to this work

https://doi.org/10.1016/j.nimb.2019.09.032
Received 12 August 2018; Received in revised form 14 June 2019; Accepted 19 September 2019
Available online 04 October 2019
0168-583X/

boundaries, dislocations, vacancies, native oxide…) and before fusion plasma induced-damage. Here, we compare the retention behavior of deuterium in single-crystal tungsten (SCW hereafter) to previous measurements [25,26] performed on recrystallized polycrystalline W samples (PCW). The initial purpose of the comparison of both types of samples was the possibility of discriminating the effects of a single type of trapping site, namely grain boundaries. The SCW sample consists in first approximation in one big grain of tungsten, i.e. with no grain boundaries. Therefore, the trapping of deuterium atoms in grain boundaries can be neglected in SCW and retention should be rather caused by the native oxide layer and, if present, dislocations and vacancies.

The paper is organized as follows. In Section 2, we present the experimental and modeling methods. Then, we describe experimental results in Section 3. The experimental results are modeled with the MHIMS-R MRE code [27] and discussed in Section 4. The summary and perspective are presented in the last section.

2. Methods

2.1. Experimental

The experiments described in the present work have been performed on two different types of tungsten samples, a single-crystal (SCW) and several poly-crystals (PCW). PCW samples were provided by A.L.M.T. Corp. (Japan) with a specified 99.99 wt% purity and with dimensions of $10 \times 10 \times 0.4\,mm^3$. Samples were delivered recrystallized and with a mirror-like mechanical polishing. They present a typical grain size of ~10 µm. The preparation process performed before introducing the samples inside ultra-high vacuum (UHV) chambers consisted in an electro-polishing procedure with a 2.5 wt% NaOH solution followed by rinsing with distilled water. Dry nitrogen was blown in order to remove eventual dust from the sample. The SCW sample was provided by Surface Preparation Laboratory (The Netherlands) and it has the dimensions of $14 \times 12 \times 2\,mm^3$. The sample was mechanically polished such that the (1 1 1) surface plane is exposed to the ion beam. No extra preparation procedure (i.e. electro-polishing) was applied in order to keep the quality of the (1 1 1) orientation. Dry nitrogen was used to remove dust.

All experiments were conducted in the CAMITER set-up located at PIIM laboratory (Aix-Marseille University – CNRS). The experimental apparatus consists in two interconnected UHV chambers: a load-lock chamber (base pressure $< 1 \times 10^{-9}$ mbar), also used for sample storage, and an implantation/thermo-desorption (TPD) chamber (base pressure $< 4 \times 10^{-10}$ mbar). To move samples between chambers, a molybdenum transfer platen is used. The platen has a surface area of $16 \times 14\,mm^2$, which makes it slightly larger than the samples and it has a circular aperture (9 mm diameter) located under the samples usual position on the platen. All samples, once introduced in the UHV implantation/TPD chamber, were subjected at least twice to a degassing procedure consisting of a linear temperature ramp of $1\,K\,s^{-1}$ up to 1300 K followed by a 10 min annealing at 1300 K. This procedure removes most of hydrocarbons impurities and leaves the native oxide of tungsten on the surface [25]. The sample is heated by a heater assembly molybdenum box with the upper face that serves as a socket for the transfer platen. Inside the box, a tungsten filament is used. The sample is heated radiatively and the temperature is controlled via a K-type thermocouple clipped on the upper face of the heater assembly at a distance of 2 mm from the platen's socket. The thermocouple signal is used to regulate the temperature with a PID controller (EUROTHERM 2604).

The deuterium implantation is performed by using an OMICRON ISE 10 ion source connected to a KREMER PS 10 control unit. An all-metal leak valve whose gas outlet is connected directly to the ion source controls the D_2 gas flow. The ions are accelerated to a kinetic energy of 500 eV and impinge the sample with an incidence angle of 45° on an elliptical projected area of $0.5\,cm^2$. The majority deuterium ion species composing the ion beam was D_2^+ (> 95%), i.e. the incident energy per deuteron is 250 eV. To such deuterium impinging conditions should corresponds a sputtering yield on the order of 10^{-5} – 10^{-4} [28,29], thus a hundredth of a W monolayer is expected to be sputtered at most in the present set of experiments i.e. ion-induced sputtering is negligible. The ion flux is determined by measuring the current on the sample with a picoammeter (Keithley 410A) and is sufficiently low to avoid the creation of D ion-induced vacancy [30]. The total incident fluence is calculated by converting the sample current into particle flux and by multiplying the particle flux with the duration of the implantation.

An implantation/TPD cycle consists in first bombarding the sample with a constant flux of $\sim 1.6 \times 10^{16}\,D^+\,m^{-2}\,s^{-1}$ for a certain duration to obtain the desired fluence. The sample is then moved to the load-lock chamber in order to degas the heater assembly on which the sample was mounted during implantation. Indeed, during ion implantation a significant neutral D_2 flux is also present, which does not adsorb on the tungsten sample (consistent with the passivation effect of oxygen towards molecular deuterium dissociation on tungsten [31]) but it does dissociate on the heater assembly. Once the heater assembly is deuterium-free and cooled down to room temperature, the sample is finally mounted back and after a given lapse of time (called the storage time hereafter), the TPD is performed. During TPD, the sample temperature is increased linearly with a ramp of $1\,K\,s^{-1}$ and its value is recorded simultaneously with HD and D_2 molecules desorption rates probed by a differentially pumped multiplexed quadrupole mass spectrometer (Hiden 3F/PIC) located about 2 mm above the sample. Deuterium retention is determined through a temporal integration of the rate of desorption of deuterium during the TPD. The implantation temperature for present measurements is 319 ± 12 K. Two sets of implantation/TPD cycles were performed for all PCW and SCW samples. In the first set of experiments, fluence was varied in the range between 6×10^{17} and $3.2 \times 10^{20}\,D^+\,m^{-2}$ and the storage time was fixed to 2.5 h. In the second set of experiments, the storage time was varied from 2.5 to 137 h after a fixed fluence of $2.81 \times 10^{19}\,D^+\,m^{-2}$. Note that NRA measurements on the SCW sample were inconclusive because of the important loss of deuterium retention in the duration necessary to transport samples to the NRA setup [25].

2.2. Modeling

The one-dimensional MRE code MHIMS-R (Migration of Hydrogen Isotopes in MetalS – Reservoir) was used in the present study. It consists in a set of three differential equations that describes the concentration of, respectively, mobile particles, trapped particles in dislocation defects and trapped particles in oxygen-vacancy cluster defects. These equations are solved for modeled samples of a thickness of 0.4 mm. The number of grid points is 1000, which are spaced according to a doubly exponential decay law. This way more than 50 grid points depict the first 5 nm below the surface and more than 200 grid points represent the depth at which deuterium atoms diffuse in PCW samples at 300 K [25]. The set of equations depicts all elementary steps encountered in experiments: 1. implantation of deuterium below the surface; 2. deuterium diffusion into the bulk or toward the surface; 3. deuterium trapping and detrapping on bulk defects during implantation, storage time and TPD. The interested reader should refer to [27] for details about the MHIMS-R code.

Diffusion, trapping and detrapping are thermally activated processes, where the process barrier $E_{barrier}$ is overcome thanks to an Arrhenius formulation of kinetic rates:

$$\nu_{process} = \nu^0_{process} \times e^{\left(-\frac{E_{barrier}}{k_B \times T}\right)}$$

and $\nu^0_{process}$ is the rate constant of the process, k_B is the Boltzmann constant and T is the sample temperature.

Table 1
List of detrapping energies from the DFT literature for different tungsten natural defects as a function of the filling-level, i.e. the number of atoms trapped at the defect.

filling- level	$E_{detrapping}$(eV)					
	grain boundary	dislocation	oxygen-vacancy	vacancy		
	Xiao & Geng [19]*	Xiao & Geng [19]*	Kong et al. [24]	Heinola et al. [21]	Fernandez et al. [23]	You et al. [22]
1	1.50	2.06	1.40	1.60	1.43	1.57
2	1.30	1.96	1.12	1.57	1.42	1.57
3	1.10	1.00	1.10	1.39	1.25	1.24
4	–	0.90	1.09	1.28	1.17	1.24
5	–	–	–	1.17	1.11	1.16
6	–	–	–	–	–	0.95

* $E_{diffusion}$ from [23] has been added to the binding energy from [19].

In the following, we set $E_{trapping} = E_{diffusion}$ with$E_{diffusion} = 0.20$ eV from the DFT study by Fernandez et al. [23]. The values used for $E_{detrapping}$ for each type of defects are from the DFT literature and are summarized in Table 1. One can notice that each type of defects in tungsten has a series of detrapping energy, which is a function of the number of deuterium atoms trapped at the defect, hereafter called the filling-level. In order to save on computational time, we applied a filling-level cutoff as soon as the detrapping energy is below 0.9 eV. Indeed, all implantations are performed at room temperature and, assuming that the $\nu^0_{detrapping}$ $10^{13}s^{-1}$ for vacancies [23] is valid for other types of tungsten bulk defects, $E_{detrapping} < 0.9eV$ corresponds to negligible trapping lifetime as compared to typical experiments duration.

3. Experimental results

Fig. 1 shows a comparison between TPD measurements obtained on SCW and PCW samples after implantation of 3.2×10^{20} D^+ m^{-2}. The TPD obtained on PCW presents a single broad peak of desorption, with the maximum located at 450 ± 50 K (the uncertainty represents the sample-to-sample variation from 3 PCW samples mounted on more than 6 different transfer platens). Similar measurements obtained on SCW reveal the presence of two desorption peaks. The characteristic of the first main peak is similar to the one observed for PCW, with a similar position in temperature for the peak maximum and roughly the same width. The second desorption peak in SCW occurs at 815 ± 30 K and its intensity remains a small fraction (~15%) of the low temperature peak in the investigated fluence range.

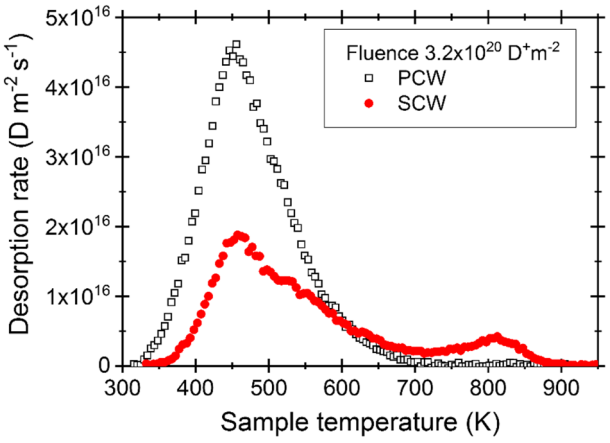

Fig. 1. TPD measurements of deuterium desorption from single-crystal (SCW) and poly-crystals (PCW) tungsten samples after implantation of 3.2×10^{20} D^+m^{-2} and a 2.5 h storage time at 300 K.

In Fig. 2 are summarized parts of the two sets of implantation/TPD series performed on SCW, as well as modeling results discussed in the next section. Fig. 2(a) shows the evolution of the TPD measurement as a function of the incident deuterium fluence, while Fig. 2(b) displays the effect of varying the storage time. When the incident deuterium fluence is increased on SCW, the two desorption peaks position evolve differently. The low temperature peak remains at a constant position, while the higher temperature peak shifts by ~25 K to a higher temperature. The fact that the temperature peak at ~450 K does not shift when the fluence is increased is in contrast with the observation made on PCW samples where a shift to lower temperature by ~30 K was observed [25,26]. These behaviors will be discussed in the next section. The effect of storage time on the low temperature desorption peak of SCW is to shift it to higher temperatures by ~30 K. This observation is consistent with measurements on PCW where a shift of ~30 K to higher temperature was observed for the single desorption peak [25,26] and it was attributed to the effect of bulk diffusion. The effect of storage time on the high temperature peak in SCW is less clear: the falling edge remains constant but the peak maximum seems to shift to higher temperature. The latter could be a result of the superposition of the high temperature peak with the falling tail of the low temperature peak that drastically diminishes with increasing the storage time.

Fig. 3 presents a comparison of integrated TPD measurements (i.e. of the deuterium retention) for SCW and PCW samples as a function of storage time. Independently of the sample microstructure (PCW or SCW), retention of deuterium appears to be dynamic at room temperature, i.e. it can be divided in two different retention zones: the short-term retention and the long-term retention zones. The short-term retention zone extends in the first 2 days of storage in UHV and displays an exponential decay of the deuterium retention. The exponential decay of the retained number of deuterium atoms in tungsten has a time constant of 22 ± 6 h for PCW and 15 ± 5 h for SCW. For storage times longer than 48 h, i.e. in the long-term retention zone, the number of trapped deuterium atoms remains essentially constant for as long as 330 h (not shown).

At a fluence of 2.81×10^{19} D^+ m^{-2} and within their uncertainties, the initial (after 2.5 h) amount of deuterium retained in PCW and SCW samples are similar. However, the amount of deuterium retention found in the long-term retention zone is different for PCW and SCW samples. PCW samples retained constantly ~3.5 ± 1% of implanted deuterium at room temperature while the SCW sample only retained ~0.7 ± 0.2%.

4. Discussion and modeling

From Fig. 3, the first obvious difference between SCW and PCW samples is their different long-term retention. On the one hand, the PCW long-term retention level is 50 ± 10% of the initial (2.5 h) short-term retention, consistently for the 3 PCW samples. On the other, the SCW long-term retention is 20 ± 4% of the initial short-term retention with ~1/3 of the long-term retention of SCW originating from the high temperature desorption peak (Fig. 2(b)). This comparison suggests that grain boundaries are in part responsible of the long-term retention of deuterium in PCW tungsten, consistent with our previous DFT-MRE modeling of PCW results [25]. The DFT energetics of Σ3 (1 1 1) grain boundaries [19] are sufficiently high for deuterium to stay retained in tungsten at 300 K indeed (see Table 1), with the first and second filling-levels being 0.4 eV and 0.2 eV, respectively, more energetic that the ~1.06 eV detrapping energy characteristic of the short-term retention decay at room temperature [26].

From Fig. 2(b), it appears that the long-term retention behavior of SCW samples originates from two different mechanisms, as seen in the two peaks structure of the TPD measurements after a storage time of 137 h. From all natural defects listed in Table 1, the long-term retention due to the ~815 K peak is consistent (thanks to a Redhead analysis

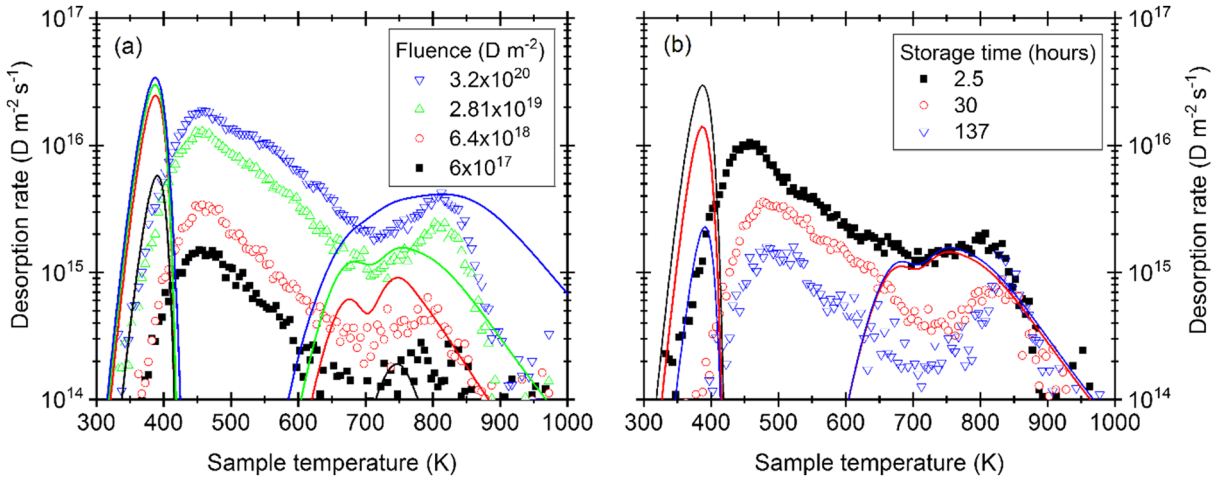

Fig. 2. TPD measurements (symbols) on SCW performed (a) 2.5 h after four different implantation fluences, and (b) for three different storage times after an implantation of 2.81×10^{19} D^+m^{-2} at room temperature. Lines are results of Model 3.

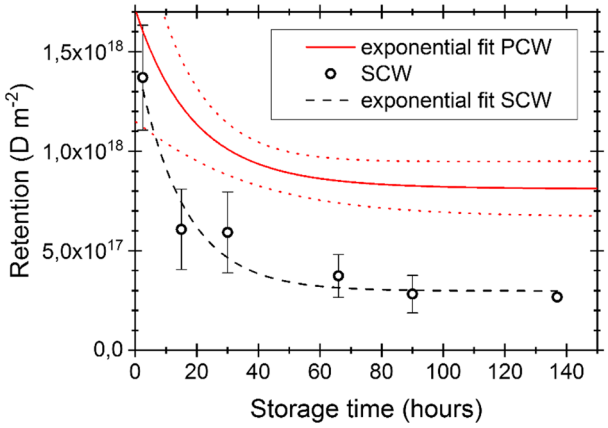

Fig. 3. Evolution of trapped deuterium in tungsten as a function of the storage time (so-called dynamic retention) at 300 K in UHV after implantation of 2.81×10^{19} D^+ m^{-2} in SCW and PCW samples. SCW uncertainties (error bars) represent the standard deviation of the mean of repeated measurements while the dashed black line shows the exponential decay fit. PCW uncertainties (dotted red lines) represent the standard deviation of the mean (red full line) of exponential decay fits performed on 3 different PCW samples. (For interpretation of the references to colour in this figure legend, the reader is referred to the web version of this article.)

[32]) only with the (1 0 0) dislocation loop's detrapping energies, in the range 1.9–2.1 eV for the first and second filling-levels [19]. Considering that the SCW sample was not electro-polished, the presence of dislocations remaining from the mechanical polishing step is well possible, in particular because it is known that annealing of intra-grain dislocations is incomplete at the temperature of our experiments [33]. We note that a poor electro-polishing of mechanically polished PCW samples give also TPD measurements with a second high temperature peak (not shown here).

The long-term retention due to the broad ~450 K peak could be explained by the multi-trapping of natural defects such as vacancies and oxygen-vacancy clusters, as seen in Table 1. These two types of defects have some filling-levels with detrapping energies in the range 1.2 – 1.6 eV allowing a stable retention at room temperature. These two defects have also some filling-levels in the 1.0 – 1.1 eV range that should exhibit the exponential decay seen in Fig. 3. Thus, vacancies and oxygen-vacancy clusters could describe both the short-term and (part of) the long-term retention in SCW and PCW samples. Considering the ratio of the long-term retention to the short-term retention in SCW (~20%), it appears that DFT energetics point to the oxygen-vacancy cluster to have the correct filling-levels distribution (~25% are > 1.2 eV) in contrary to the vacancy defect which should have a weaker dynamic retention at room temperature (~80% are > 1.2 eV).

So far, we discussed qualitatively the experimental results in the light of the DFT literature. In the following, a more quantitative analysis of SCW results is realized using MRE models that includes these DFT inputs (see Section 2.2). Note that we will present DFT-MRE models that include only dislocations and oxygen-vacancy clusters since there are no grain boundaries in SCW and vacancy defects did not lead to satisfactory results. The reader that would be interested in the details of the DFT-MRE modeling of PCW samples should refer to Hodille et al. [25].

We first considered the scenario where the only naturally defective part of the sample is a 4 nm thick layer containing oxygen-vacancy clusters (Model 1, Table 2), since we have measured with Auger electron spectroscopy the presence of a native oxide layer in our experimental conditions at the surface of both SCW and PCW samples [25]. This thin layer of oxygen-vacancy clusters should be seen as a surrogate for modeling the tungsten native oxide layer because its amorphous

Table 2
List of parameters used for each (DFT-) MRE model to simulate the experimental retention.

Model	type of defect/trap											
	oxygen-vacancy cluster						dislocation					
	filling-levels	energy (eV)				ρ_{trap}	filling-levels	energy (eV)				ρ_{trap}*
Model 1	4	1.40	1.12	1.10	1.09	1.35	0	–	–	–	–	–
Model 2	4	1.40	1.12	1.10	1.09	0.5	4	2.06	1.96	1.00	0.90	0.17
Model 3	1	1.08	–	–	–	4.5	4	2.06	1.96	1.00	0.90	0.03

* ρ_{trap} is the density of trapping sites expressed in atomic fraction of $10^{-3} \times \rho_W$ where the tungsten density ρ_W is 6.3×10^{28} m^{-3}.

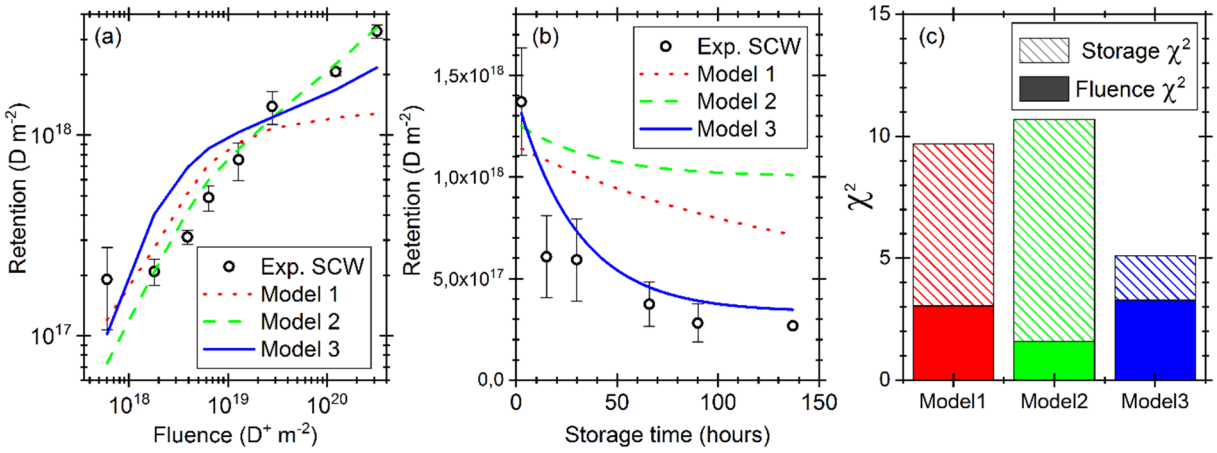

Fig. 4. Three different MHIMS-R models compared to experimental results on SCW for (a) the deuterium retention as a function of fluence and (b) the dynamic retention of deuterium. Circles represent experimental data while lines are models results. (c) Pearson's chi-squared test obtained by comparing experimental and modeling results.

nature precludes the use of periodic-DFT to determine its energetics. In order to minimize the deviation between SCW experimental results and modeling (evaluated by the Pearson's chi-squared test, χ^2, shown in Fig. 4(c)), we have varied only one free parameter: the trap density ρ_{oxide}. This parameter was varied between 0.01 and $5.00 \times 10^{-3} \times \rho_W$ by steps of $0.01 \times 10^{-3} \times \rho_W$. With a trap density $\rho_{oxide} = 1.35 \times 10^{-3} \times \rho_W$, where ρ_W is the tungsten density (6.3×10^{28} m^{-3}), Model 1 is able to reproduce the retention behavior as a function of fluence only up to 2.8×10^{19} D$^+$ m^{-2} (Fig. 4(a)). For higher fluence, the modeled retention appears to level-off, accentuating the experimental retention kink at 2.8×10^{19} D$^+$ m^{-2}. This leveling-off indicates that the oxide layer is saturated. When increasing the value of ρ_{oxide}, the position of the kink to leveling-off shifts to higher fluences, indeed. More importantly, Model 1 is able to predict only qualitatively the short term retention behavior, with a longer time constant of the exponential decay though it is consistent with the energetics of oxygen-vacancy cluster filling-levels 2, 3 and 4. The long-term retention behavior, i.e. the constant retention as a function of time is not obtained with Model 1 for the typical storage time probed in the experiments. The reason could lie with the presence of a double trap system, as suggested by the experimental TPD results of Fig. 2(b): a first trap with low detrapping energies responsible of the initial exponential decay of the short-term retention, and a second trap with high detrapping energies playing the role of a deuterium reservoir for the long-term retention. As argued at the beginning of this section, the presence of a high temperature desorption peak (~815 K) could be related to the presence of dislocations. Thus, in the second model (Model 2) we consider both oxygen-vacancy clusters and dislocations traps using detrapping energies from the DFT literature.

In Model 2, the trap density of the oxygen-vacancy clusters ρ_{oxide} and of the dislocations $\rho_{dislocation}$ are the only two free parameters. While the oxide layer has the same 4 nm thickness than in Model 1, for dislocations we set an uniform density throughout the material. As shown by the green dashed curve in Fig. 4(a), Model 2 is able to model quantitatively the fluence behavior of retention as well as the retention kink. On the contrary, it is not able to reproduce quantitatively the retention as function of storage time. Nevertheless, qualitatively, one can note that the addition of dislocation traps induced the appearance of a long-term constant retention behavior. These results have been obtained using traps density of $\rho_{oxide} = 0.5 \times 10^{-3} \times \rho_W$ and $\rho_{dislocation} = 0.17 \times 10^{-3} \times \rho_W$, i.e. the two traps density are quite similar. The consequence is that the relative ratio of TPD peaks in Model 2 is close to 1:1 in peak height (not shown here) i.e. very dissimilar with experimental observations where a ~6:1 ratio is found (Figs. 1 and 2). We stress that we have varied, with a step of $0.01 \times 10^{-3} \times \rho_W$, ρ_{oxide} between 0.5 and $1.5 \times 10^{-3} \times \rho_W$ and $\rho_{dislocation}$ in the range 0.025 and $0.17 \times 10^{-3} \times \rho_W$. Other couples of ($\rho_{oxide}$, $\rho_{dislocation}$) values can allow to slightly improve the overall model results (< 10% for the total χ^2), by reducing the χ^2 for storage time experiments but by increasing the χ^2 for fluence experiments.

Fig. 4(c) shows that for both Model 1 and Model 2, most of the deviation between experiments and modeling is coming from the too slow dynamic retention (i.e. Storage χ^2) of the oxygen-vacancy clusters model of the native oxide. Using simple first-order Arrhenius kinetics with $\nu^0_{detrapping} = 10^{13} s^{-1}$, one can evaluate that detrapping energies ≥ 1.10 eV (as in the case of DFT oxygen-vacancy traps) at room temperature will not allow a "fast enough" releasing of deuterium atoms, therefore preventing a good fit of the short-term retention behavior. Given the exponential dependence with detrapping energy of first-order Arrhenius isothermal kinetics, just a few percent change in detrapping energies for the oxide trap would induce a strong improvement of modeling results. Comparing vacancy trap energetics in Table 1 between several authors, it is evident that DFT energetics accuracy are within 10%. Thus, limitations of Model 1 and 2 could be due in part to DFT accuracy in determining correct energetics of the oxygen-vacancy clusters for modeling the native oxide. Or, Model 1 and 2 limitations could originate from the choice of oxygen-vacancy clusters to model the amorphous native oxide layer.

The topic of modeling an impurity layer in tungsten has been recently discussed by Wang et al. [34] in the case of implanted nitrogen layers. Combining DFT calculations and a McNabb-Foster formulation of hydrogen effective diffusivity, these authors found that both interstitial nitrogen and nitrogen-vacancy clusters are able to reduce the hydrogen effective diffusivity in tungsten, i.e. the nitrogen-enriched layer of W acts as a diffusion barrier for hydrogen desorption. We postulate that an oxygen-enriched layer could behave similarly to the nitrogen impurities described by Wang *et al.* since the filling-levels – detrapping energies structure is quite similar. Such consideration pushes us to explore a third scenario (Model 3) putting aside DFT values for the native oxide layer and using instead an ersatz of an effective diffusion barrier layer. We have chosen to vary only one parameter, the detrapping energy of a single filling-level defect representing the native oxide layer, keeping fixed the diffusion energy to 0.2 eV. This was a practical choice aimed at simplifying the implementation of the diffusion barrier in the current version of MHIMS-R. We varied ρ_{oxide} and $\rho_{dislocation}$ in the same range than in model 2 with the same $0.01 \times 10^{-3} \times \rho_W$ step. Regarding the single detrapping energy for the oxide, we probed the range 0.95 – 1.20 eV with a step of 0.01 eV. A good agreement between experimental and modeling results has been obtained by using (ρ_{oxide}, $\rho_{dislocation}$) = $(4.5,\ 0.03) \times 10^{-3} \times \rho_W$ and a

single detrapping energy for the native oxide layer of 1.08 eV. The dynamic retention is reproduced quantitatively (Fig. 4(b)) as expressed in the storage χ^2 that is reduced by 75% with respect to results of Model 2 (Fig. 4(c)). In term of fluence experiments, modeling results are still in fairly good agreement with experimental ones (Fig. 4(a)), i.e. within a factor of 2, even if parameter choices worsen the fluence χ^2 accentuating and bringing forward the kink at 5×10^{18} D m^{-2}. Thus, Model 3 validates our initial hypothesis of a double trap mechanism (oxides + dislocations) in the case of SCW sample. In particular, we have shown that the native oxide layer should be responsible for most of the short-term (dynamic) retention while dislocations account significantly for the long-term retention.

We stress that for all present models, the modeled TPD measurements reproduce only qualitatively the experimental observation (Fig. 2). First, the temperature position of TPD peaks is different between models and experiments by at most ~70 K. We recall that our experimental peak positions uncertainty spans a range of temperature of 70–100 K because thermocouple measurements are not directly done on SCW or PCW samples, but 2 mm away. We believe that the experimental temperature measurement setup is the main reason for discrepancy and we are planning to fix this issue in future studies. Second, we discuss the effect of implantation fluence on the experimental position of peaks maximum. The low temperature desorption peak at ~450 K, common to SCW and PCW samples, appears to behave differently when varying fluence on both type of samples: while there is a shift towards lower temperature on PCW samples, it stays constant in position for the SCW sample. We previously attributed the temperature shift in PCW to the filling-levels structure of grain boundaries traps [25,26]. The absence of the shift for the single-crystal experimental experiments is consistent with the absence of grain boundaries. However, the filling-levels structure of the oxygen-vacancy clusters we used in Model 1 and Model 2 give also a shift of the ~450 K TPD peak to lower temperature by ~70 K with increasing fluence (not shown). This discrepancy with the experimental observation suggests that the oxygen-vacancy clusters is not a satisfactory surrogate for the native oxide layer. In contrast, the description of the native oxide layer as a diffusion barrier used in Model 3 allows reproducing the experimental observation of an absence of shift of the ~450 K peak in SCW (Fig. 2(a)). This diffusion barrier model is obviously an effective model that demeans the spirit of DFT-MRE models we recently developed. However, it seems to be necessary for amorphous layered materials considering the use of periodic conditions in current DFT studies. Finally, we note that the ~815 K peak shift to high temperature with increasing fluence is well reproduced by the DFT-MRE model of dislocations. This could seem surprising at first since the filling-levels structure of dislocations would suggest the opposite behavior. However, comparison of experimental and modeling results in Fig. 2(b) shows a more complex situation. For fluence in the 10^{18}–10^{19} D$^+$ m^{-2} range, the ~815 K peak does shift to lower temperature in the model, which could explain the broad increase of desorption rate in the 650–750 K range in the experiments. For higher fluence, i.e. for longer implantation duration, the effect of saturation of the local dislocations density and the subsequent displacement of the deuterium front further in the bulk seems to occur [27], thus explaining the observed ~815 K TPD peak shift to higher temperature. We note that the position of the ~450 K TPD peak within the native oxide diffusion barrier (Model 3) is not affected by the increased fluence, which is a signature of its near-surface localization with a 4 nm modeled thickness.

5. Summary and perspectives

We presented a comparative study of the dynamic retention of deuterium in single-crystal (SCW) and poly-crystals (PCW) of tungsten samples. We found that both SCW and PCW exhibit a similar initial deuterium retention that decays exponentially with a time constant of ~18 h, the so-called short-term retention. After ~48 h, the amount of deuterium in PCW and SCW samples remains constant (long-term retention) for as long as 330 h. However, PCW long-term retention is found to be systematically higher than SCW long-term retention, confirming the trapping effect of grain boundaries at room temperature that we previously predicted [25]. Using the MHIMS-R code to model the SCW results, we tested three different MRE models that use DFT inputs of multi-detrapping energies for two defects: dislocations and oxygen-vacancy clusters. The latter type of defect was used as a surrogate for modeling the native oxide surface layer observed experimentally in SCW (and PCW). The oxygen-vacancy clusters DFT-MRE model (Model 1) was able to reproduce qualitatively the short-term retention exponential behavior. It was argued that one would need to change the DFT detrapping energies by only a few percent in order to attain a quantitative agreement, which would be reasonable considering the current DFT accuracy achieved in the literature. The addition of oxygen-vacancy clusters and dislocations defects in the DFT-MRE Model 2 allowed to reproduce qualitatively the short- and long-term retention as well as to obtain the two desorption peaks structure observed experimentally. Model 3 was able to achieve near-quantitative agreement with all retention experiments but at the expense of using an effective diffusivity of deuterium in the oxide layer, i.e. this model was only partially a DFT-MRE model. We motivated this effective model of the native oxide by taking into account its amorphous nature, which is incompatible with periodic DFT methods.

In short, studying a single-crystal allowed demonstrating the universal nature of dynamic deuterium retention in tungsten. DFT-MRE models of SCW and PCW results [25] permitted to show that this dynamic retention can originate for a variety of defects: oxides, grain boundaries, vacancies…, that should all contributes also to the long-term retention. In order to assess the relative weight of these defects in deuterium retention in tungsten, it is necessary to make progress on several fronts. First, additional DFT studies are needed to assess the detrapping energies of various grain boundaries and dislocations geometries. Second, a more systematic estimation of DFT uncertainties would be valuable to estimate the energy range that DFT-MRE modeler can explore around these input parameters. From the experimental side, it is important to assess the confidence that one has with the sample temperature measurement. In that prospect, we are currently designing a new heater assembly that will allow the direct measurement of the sample surface temperature on transferable samples. Furthermore, surface preparation appears to be an important step in obtaining tungsten samples that are simpler to analyze: electro-polishing may be an important step to remove surface polishing induced-defects as we have seen in SCW and PCW samples. Finally, the retention properties of the native oxide layer need to be studied systematically, both experimentally and theoretically. Measuring the deuterium retention in crystalline tungsten oxide would be a path that joint experimental – modeling effort could follow.

Acknowledgments

The project leading to this publication has received funding from Excellence Initiative of Aix-Marseille University – A*Midex, a French “Investissements d’Avenir” programme. This work has been carried out within the framework of the EUROfusion Consortium and has received funding from the Euratom research and training programme 2014–2018 under grant agreement No 633053. The views and opinions expressed herein do not necessarily reflect those of the European Commission.

References

[1] M. Kaufmann, R. Neu, Tungsten as first wall material in fusion devices, Fusion Eng. Des. 82 (2007) 521–527, https://doi.org/10.1016/j.fusengdes.2007.03.045.
[2] J. Paméla, G.F. Matthews, V. Philipps, R. Kamendje, An ITER-like wall for JET, J. Nucl. Mater. 363–365 (2007) 1–11, https://doi.org/10.1016/j.jnucmat.2006.12.

056.
[3] G.D. Temmerman, T. Hirai, R.A. Pitts, The influence of plasma-surface interaction on the performance of tungsten at the ITER divertor vertical targets, Plasma Phys. Control. Fusion. 60 (2018) 044018, , https://doi.org/10.1088/1361-6587/aaaf62.
[4] J. Roth, E. Tsitrone, T. Loarer, V. Philipps, S. Brezinsek, A. Loarte, G.F. Counsell, R.P. Doerner, K. Schmid, O.V. Ogorodnikova, R.A. Causey, Tritium inventory in ITER plasma-facing materials and tritium removal procedures, Plasma Phys. Control. Fusion. 50 (2008) 103001, , https://doi.org/10.1088/0741-3335/50/10/103001.
[5] G. De Temmerman, M.J. Baldwin, D. Anthoine, K. Heinola, A. Jan, I. Jepu, J. Likonen, C.P. Lungu, C. Porosnicu, R.A. Pitts, Efficiency of thermal outgassing for tritium retention measurement and removal in ITER, Nucl. Mater. Energy. 12 (2017) 267–272, https://doi.org/10.1016/j.nme.2016.10.016.
[6] R.A. Causey, Hydrogen isotope retention and recycling in fusion reactor plasma-facing components, J. Nucl. Mater. 300 (2002) 91–117, https://doi.org/10.1016/S0022-3115(01)00732-2.
[7] C.H. Skinner, A.A. Haasz, V.K. Alimov, N. Bekris, R.A. Causey, R.E.H. Clark, J.P. Coad, J.W. Davis, R.P. Doerner, M. Mayer, A. Pisarev, J. Roth, T. Tanabe, Recent advances on hydrogen retention in ITER's plasma-facing materials: beryllium, carbon, and tungsten, Fusion Sci. Technol. 54 (2008) 891–945, https://doi.org/10.13182/FST54-891.
[8] T. Tanabe, Review of hydrogen retention in tungsten, Phys. Scr. T159 (2014) 014044, , https://doi.org/10.1088/0031-8949/2014/T159/014044.
[9] G.-H. Lu, H.-B. Zhou, C.S. Becquart, A review of modelling and simulation of hydrogen behaviour in tungsten at different scales, Nucl. Fusion. 54 (2014) 086001, , https://doi.org/10.1088/0029-5515/54/8/086001.
[10] O.V. Ogorodnikova, J. Roth, M. Mayer, Deuterium retention in tungsten in dependence of the surface conditions, J. Nucl. Mater. 313–316 (2003) 469–477 16/S0022-3115(02)01375-2.
[11] G.R. Longhurst, Tmap7 User Manual, Idaho National Laboratory (INL), 2008. http://www.osti.gov/scitech/biblio/952013-lrxIhW/ (accessed December 14, 2016).
[12] K. Schmid, V. Rieger, A. Manhard, Comparison of hydrogen retention in W and W/Ta alloys, J. Nucl. Mater. 426 (2012) 247–253, https://doi.org/10.1016/j.jnucmat.2012.04.003.
[13] C. Sang, J. Sun, X. Bonnin, L. Wang, H. Du, Y. Huang, D. Wang, Modelling of hydrogen isotope retention in the tungsten divertor of EAST during ELMy H-mode, Fusion Eng. Des. 89 (2014) 2214–2219, https://doi.org/10.1016/j.fusengdes.2014.01.040.
[14] A. Hu, A. Hassanein, Modeling hydrogen isotope behavior in fusion plasma-facing components, J. Nucl. Mater. 446 (2014) 56–62, https://doi.org/10.1016/j.jnucmat.2013.11.033.
[15] E.A. Hodille, X. Bonnin, R. Bisson, T. Angot, C.S. Becquart, J.M. Layet, C. Grisolia, Macroscopic rate equation modeling of trapping/detrapping of hydrogen isotopes in tungsten materials, J. Nucl. Mater. 467 (2015) 424–431, https://doi.org/10.1016/j.jnucmat.2015.06.041.
[16] J. Guterl, R.D. Smirnov, S.I. Krasheninnikov, M. Zibrov, A.A. Pisarev, Theoretical analysis of deuterium retention in tungsten plasma-facing components induced by various traps via thermal desorption spectroscopy, Nucl. Fusion. 55 (2015) 093017, , https://doi.org/10.1088/0029-5515/55/9/093017.
[17] E.A. Hodille, E. Bernard, S. Markelj, J. Mougenot, C.S. Becquart, R. Bisson, C. Grisolia, Estimation of the tritium retention in ITER tungsten divertor target using macroscopic rate equations simulations, Phys. Scr. T170 (2017) 014033, , https://doi.org/10.1088/1402-4896/aa8787.
[18] H.-B. Zhou, Y.-L. Liu, S. Jin, Y. Zhang, G.-N. Luo, G.-H. Lu, Investigating behaviours of hydrogen in a tungsten grain boundary by first principles: from dissolution and diffusion to a trapping mechanism, Nucl. Fusion. 50 (2010) 025016, , https://doi.org/10.1088/0029-5515/50/2/025016.
[19] W. Xiao, W.T. Geng, Role of grain boundary and dislocation loop in H blistering in W: a density functional theory assessment, J. Nucl. Mater. 430 (2012) 132–136, https://doi.org/10.1016/j.jnucmat.2012.07.013.
[20] Y.-L. Liu, Y. Zhang, H.-B. Zhou, G.-H. Lu, F. Liu, G.-N. Luo, Vacancy trapping mechanism for hydrogen bubble formation in metal, Phys. Rev. B. 79 (2009) 172103, , https://doi.org/10.1103/PhysRevB.79.172103.
[21] K. Heinola, T. Ahlgren, K. Nordlund, J. Keinonen, Hydrogen interaction with point defects in tungsten, Phys. Rev. B. 82 (2010) 094102, , https://doi.org/10.1103/PhysRevB.82.094102.
[22] Y.-W. You, X.-S. Kong, X.-B. Wu, Y.-C. Xu, Q.F. Fang, J.L. Chen, G.-N. Luo, C.S. Liu, B.C. Pan, Z. Wang, Dissolving, trapping and detrapping mechanisms of hydrogen in bcc and fcc transition metals, AIP Adv. 3 (2013) 012118, , https://doi.org/10.1063/1.4789547.
[23] N. Fernandez, Y. Ferro, D. Kato, Hydrogen diffusion and vacancies formation in tungsten: density Functional Theory calculations and statistical models, Acta Mater. 94 (2015) 307–318, https://doi.org/10.1016/j.actamat.2015.04.052.
[24] X.-S. Kong, Y.-W. You, Q.F. Fang, C.S. Liu, J.-L. Chen, G.-N. Luo, B.C. Pan, Z. Wang, The role of impurity oxygen in hydrogen bubble nucleation in tungsten, J. Nucl. Mater. 433 (2013) 357–363, https://doi.org/10.1016/j.jnucmat.2012.10.024.
[25] E.A. Hodille, F. Ghiorghiu, Y. Addab, A. Založnik, M. Minissale, Z. Piazza, C. Martin, T. Angot, L. Gallais, M.-F. Barthe, C.S. Becquart, S. Markelj, J. Mougenot, C. Grisolia, R. Bisson, Retention and release of hydrogen isotopes in tungsten plasma-facing components: the role of grain boundaries and the native oxide layer from a joint experiment-simulation integrated approach, Nucl. Fusion. 57 (2017) 076019, , https://doi.org/10.1088/1741-4326/aa6d24.
[26] R. Bisson, S. Markelj, O. Mourey, F. Ghiorghiu, K. Achkasov, J.-M. Layet, P. Roubin, G. Cartry, C. Grisolia, T. Angot, Dynamic fuel retention in tokamak wall materials: An in situ laboratory study of deuterium release from polycrystalline tungsten at room temperature, J. Nucl. Mater. 467 (2015) 432–438, https://doi.org/10.1016/j.jnucmat.2015.07.028.
[27] E.A. Hodille, Y. Ferro, N. Fernandez, C.S. Becquart, T. Angot, J.M. Layet, R. Bisson, C. Grisolia, Study of hydrogen isotopes behavior in tungsten by a multi trapping macroscopic rate equation model, Phys. Scr. T167 (2016) 014011, , https://doi.org/10.1088/0031-8949/2016/T167/014011.
[28] W. Eckstein, Sputtered Energy Coefficient and Sputtering Yield, Max-Planck-Institut für Plasmaphysik, Garching, 2011 http://edoc.mpg.de/display.epl?mode=doc&id=574473&col=33&grp=1311#cb.
[29] K. Sugiyama, K. Schmid, W. Jacob, Sputtering of iron, chromium and tungsten by energetic deuterium ion bombardment, Nucl. Mater. Energy. 8 (2016) 1–7, https://doi.org/10.1016/j.nme.2016.05.016.
[30] E.A. Hodille, N. Fernandez, Z.A. Piazza, M. Ajmalghan, Y. Ferro, Hydrogen supersaturated layers in H/D plasma-loaded tungsten: a global model based on thermodynamics, kinetics and density functional theory data, Phys. Rev. Mater. 2 (2018) 093802, , https://doi.org/10.1103/PhysRevMaterials. 2.093802.
[31] J.E. Whitten, R. Gomer, The coadsorption of H and O on the W (110) plane, Surf. Sci. 409 (1998) 16–26. doi:16/S0039-6028(98)00188-5.
[32] P.A. Redhead, Thermal desorption of gases, Vacuum. 12 (1962) 203–211, https://doi.org/10.1016/0042-207X(62)90978-8.
[33] R.A. Anderl, D.F. Holland, G.R. Longhurst, R.J. Pawelko, C.L. Trybus, C.H. Sellers, Deuterium transport and trapping in polycrystalline tungsten, Fusion Technol. 21 (1992) 745–752, https://doi.org/10.13182/FST92-A29837.
[34] S. Wang, X.-S. Kong, X. Wu, Q.F. Fang, J.-L. Chen, G.-N. Luo, C.S. Liu, Effects of nitrogen on hydrogen retention in tungsten: First-principles calculations, J. Nucl. Mater. 459 (2015) 143–149, https://doi.org/10.1016/j.jnucmat.2015.01.025.